

Layer-dependent spin-orbit torques generated by the centrosymmetric transition metal dichalcogenide β -MoTe₂

Gregory M. Stiehl,¹ Ruofan Li,¹ Vishakha Gupta,¹ Ismail El Baggari,¹

Shengwei Jiang,² Hongchao Xie,² Lena F. Kourkoutis,^{2,3} Kin Fai

Mak,^{1,2,3} Jie Shan,^{1,2,3} Robert A. Buhrman,² and Daniel C. Ralph^{1,3}

¹*Department of Physics, Cornell University, Ithaca, NY 14853, USA*

²*School of Applied and Engineering Physics,
Cornell University, Ithaca, NY 14853, USA*

³*Kavli Institute at Cornell, Cornell University, Ithaca, NY 14853, USA*

(Dated: June 5, 2019)

Abstract

Single-crystal materials with sufficiently low crystal symmetry and strong spin-orbit interactions can be used to generate novel forms of spin-orbit torques on adjacent ferromagnets, such as the out-of-plane antidamping torque previously observed in WTe₂/ferromagnet heterostructures. Here, we present measurements of spin-orbit torques produced by the low-symmetry material β -MoTe₂, which unlike WTe₂ retains bulk inversion symmetry. We measure spin-orbit torques on β -MoTe₂/Permalloy heterostructures using spin-torque ferromagnetic resonance as a function of crystallographic alignment and MoTe₂ thickness down to the monolayer limit. We observe an out-of-plane antidamping torque with a spin torque conductivity as strong as 1/3 of that of WTe₂, demonstrating that the breaking of bulk inversion symmetry in the spin-generation material is not a necessary requirement for producing an out-of-plane antidamping torque. We also measure an unexpected dependence on the thickness of the β -MoTe₂ – the out-of-plane antidamping torque is present in MoTe₂/Permalloy heterostructures when the β -MoTe₂ is a monolayer or trilayer thick, but goes to zero for devices with bilayer β -MoTe₂.

Spin-orbit torques represent one of the most promising methods for manipulating emerging magnetic memory technologies [1]. When a charge current is applied to a material with large spin-orbit coupling, such as a heavy metal [2–7], topological insulator [8, 9], or transition metal dichalcogenide (TMD) [10–16], a spin current generated through mechanisms such as the spin Hall or Rashba-Edelstein effects can be used to exert a torque on an adjacent ferromagnet. Recent work from several research groups has focused on understanding how a controlled breaking of symmetry in a spin-generating material / ferromagnet heterostructure can be used to tune the direction of the observed spin-orbit torques for optimal switching of magnetic devices [12–14, 17–24]. For instance, the presence of magnetic order within a spin-generation layer can allow current-generated spin directions that are typically forbidden for highly-symmetric non-magnetic metals [17–20]. Similarly, our group has shown that by using WTe_2 as the spin-source material, a TMD with a low-symmetry crystal structure, it is possible to generate an out-of-plane antidamping torque [12, 13] – the component of torque required for the most efficient mode of switching for magnets with perpendicular magnetic anisotropy, but forbidden in higher-symmetry materials. Only one other material, SrRuO_3 , has been shown to generate an out-of-plane antidamping spin-orbit torque [20], arising from symmetry breaking associated with magnetic order. Many questions remain regarding the mechanism and necessary conditions for generating a strong out-of-plane antidamping torque.

In this work, we study the spin-orbit torques generated in TMD/ferromagnet heterostructures with a crystal symmetry that is distinct from WTe_2 in an important way – inversion symmetry is intact in the bulk of the spin-generation material. We perform spin-torque measurements of TMD/ferromagnet heterostructures with the monoclinic phase (β) of MoTe_2 as the spin-source material. Using spin-torque ferromagnetic resonance (ST-FMR), we measure the spin-orbit torques as a function of crystal axis alignment and TMD thickness down to the monolayer limit. We find that an out-of-plane antidamping torque is present in β - MoTe_2 /ferromagnet heterostructures even though inversion symmetry is intact in the MoTe_2 bulk. Interestingly, we find that while this out-of-plane antidamping torque is strong in both monolayer and trilayer thick MoTe_2 devices, the observed torque goes to zero in bilayer-thick MoTe_2 .

The monoclinic (β or $1T'$) phase of MoTe_2 provides a unique opportunity to probe the symmetries relevant for the generation of novel spin-orbit torques, in that the individual

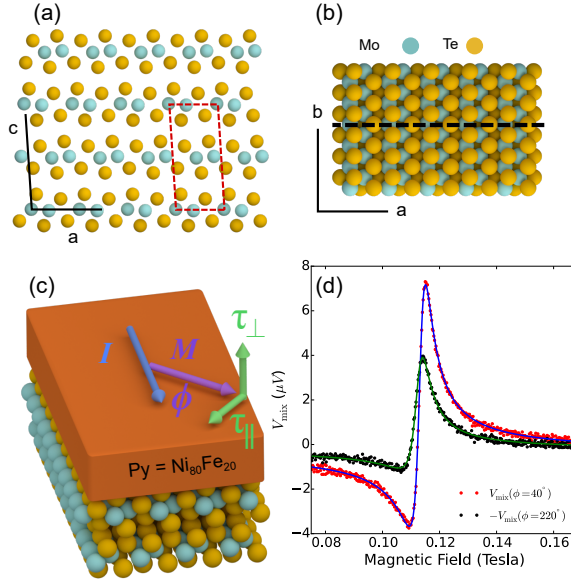


FIG. 1. a and b) Structure of the MoTe_2 crystal in the monoclinic (β or $1T'$) phase (a) depicted in the a - c plane for which the mirror plane is within the page and the Mo chains run into the page and (b) in the a - b plane where the a - c mirror plane is depicted by the dashed black line. c) Geometry of the induced spin-orbit torques in our MoTe_2/Py heterostructures. The applied current is defined as being in the \hat{x} direction. d) The measured mixing voltage, V_{mix} , as a function of applied magnetic field for Device 1, $\text{MoTe}_2(\text{monolayer}) / \text{Py}(6 \text{ nm})$, where the current is applied perpendicular to the mirror plane and the field applied at an angle of 40° (red) and 220° (black), showing a clear lack of two-fold rotational symmetry in the generated spin-orbit torques. Fits using a sum of symmetric and antisymmetric Lorentzians, shown in blue and green respectively, show good agreement with the data. The applied microwave power is 5 dBm at 9 GHz.

monolayers of $\beta\text{-MoTe}_2$ are isostructural to WTe_2 monolayers, but are stacked such that inversion symmetry is maintained in the bulk crystal. Bulk $\beta\text{-MoTe}_2$ has the space group $P2_1/m$, (#11), with a screw axis along the Mo chain and a mirror plane perpendicular to the screw axis (Fig. 1a) [25]. Similar to WTe_2 , however, the surface symmetry is limited to just one mirror plane perpendicular to the Mo chain shown in Fig. 1b.

To fabricate our samples we exfoliate flakes of bulk $\beta\text{-MoTe}_2$ crystal (provided by HQ graphene) onto high resistivity silicon / silicon oxide wafers, where the last step of the exfoliation process is carried out under vacuum ($< 10^{-6}$ torr) in the load lock of our sputtering system. We then use grazing angle sputtering to deposit 6 nm of our ferromagnet,

Permalloy (Py=Ni₈₀Fe₂₀), and subsequently cap the films with 2 nm of Al that is oxidized upon exposure to air. The equilibrium direction of the Py magnetic moment is within the sample plane. Flakes are identified for patterning by optical and atomic force microscopy (AFM); we select regions of flakes that are clean (no tape residue) and atomically flat (<300 pm roughness) with no monolayer steps over the entire region from which devices will be fabricated. The thicknesses of the β -MoTe₂ flakes can be accurately determined by AFM (with a layer step-height of ~ 0.7 nm). Samples are then patterned into device structures using electron beam lithography and ion mill etching. Electrical contact is made using 5 nm Ti/75 nm Pt electrodes. The data presented in the main text of this work are all taken at room temperature. We have confirmed that all our devices (down to the monolayer limit) are in the β -MoTe₂ phase at room temperature by polarized Raman spectroscopy (see Appendix). We have also used polarized Raman spectroscopy to determine the crystallographic orientation of each device with respect to the applied current direction [26–32].

For the ST-FMR measurements [4, 8, 12], we use a ground-signal-ground type device structure, in which we apply a GHz frequency current to the MoTe₂/Py bar through the capacitive branch of a bias tee. We set the angle of the applied magnetic field with respect to the current direction, ϕ , and sweep the magnitude of that field to tune the ferromagnet through its resonance condition while measuring the resultant DC mixing voltage at the inductive end of the bias tee. The mixing voltage, V_{mix} , as a function of field magnitude can be fit accurately as the sum of symmetric and antisymmetric Lorentzians. The amplitudes of those Lorentzians are related to the in-plane (τ_{\parallel}) and out-of-plane (τ_{\perp}) torques on the ferromagnet, respectively, by [4, 8, 12]:

$$V_S = -\frac{I_{RF}}{2} \frac{dR}{d\phi} \frac{1}{\alpha_G \gamma (2B_0 + \mu_0 M_{eff})} \tau_{\parallel} \quad (1)$$

$$V_A = -\frac{I_{RF}}{2} \frac{dR}{d\phi} \frac{\sqrt{1 + \mu_0 M_{eff}/B_0}}{\alpha_G \gamma (2B_0 + \mu_0 M_{eff})} \tau_{\perp}, \quad (2)$$

where R is the device resistance, $dR/d\phi$ is due to the anisotropic magnetoresistance in the Py, $\mu_0 M_{eff}$ is the out-of-plane demagnetization field, B_0 is the resonance field, I_{RF} is the microwave current in the bilayer, α_G is the Gilbert damping coefficient and γ is the gyromagnetic ratio. Figure 1d shows V_{mix} at two applied field angles, 40° and 220°, for one of our devices (Device 1, containing one monolayer of MoTe₂) where the applied current in the device is perpendicular to the MoTe₂ mirror plane and the 220° trace has been multiplied by

-1 for comparison. Fits to the data using a sum of symmetric and antisymmetric Lorentzians show good agreement.

In high symmetry materials such as Pt, the generated spin-orbit torques are limited by symmetry to consist of an out-of-plane field-like torque, $\vec{\tau}_A \propto \hat{m} \times \hat{y}$, and an in-plane antidamping torque, $\vec{\tau}_S \propto \hat{m} \times (\hat{m} \times \hat{y})$, which both have a dependence on the magnetization direction $\propto \cos(\phi)$ [33]. That the V_{mix} data in Fig. 1d are not identical up to a minus sign for the two applied field angles indicates that torques in the $\beta\text{-MoTe}_2/\text{Py}$ system do not preserve two-fold symmetry, *i.e.* an out-of-plane antidamping torque, $\vec{\tau}_B \propto \hat{m} \times (\hat{m} \times \hat{z})$, may be present. Note that we define the applied current as always being in the \hat{x} direction (Fig. 1c).

To determine the components of current-induced torque, we analyze the extracted fit parameters V_S and V_A as a function of applied field angle. Representative data for Device 1 are shown in Fig. 2a and b. If only the torques τ_A and τ_S are present, V_A and V_S will be $\propto \sin(2\phi) \cos(\phi)$, where the $\propto \sin(2\phi)$ arises from $dR/d\phi$ due to the anisotropic magnetoresistance of the Py. However, the angular dependence of V_A (Fig. 2b) cannot be described with this simple overall angular dependence $\propto \sin(2\phi) \cos(\phi)$. To extract the other out-of-plane torques present in the system, we fit the angular dependence of V_A as:

$$V_A = \sin(2\phi)[A \cos(\phi) + B + C \sin(\phi)]. \quad (3)$$

The fit parameter B corresponds to torques $\vec{\tau}_B \propto \hat{m} \times (\hat{m} \times \hat{z})$. The fit parameter C corresponds to torques $\vec{\tau}_C \propto \hat{m} \times \hat{x}$ – the torque with a Dresselhaus-like symmetry observed in TaTe_2 and WTe_2 that likely arises from the in-plane resistance anisotropy of the low-symmetry TMD [16]. For Device 1, we find a ratio $B/A = 0.302 \pm 0.001$ indicating a sizable out-of-plane antidamping torque, whereas C is zero to within experimental uncertainty.

We may similarly fit V_S to test for additional in-plane torques:

$$V_S = \sin(2\phi)[S \cos(\phi) + T + U \sin(\phi)], \quad (4)$$

where T corresponds to torques $\vec{\tau}_T \propto \hat{m} \times \hat{z}$, and U gives torques $\vec{\tau}_U \propto \hat{m} \times (\hat{m} \times \hat{x})$. In Device 1, T and U are zero within experimental uncertainty. However, other samples show non-zero values for T and U as discussed below.

When a spin-generation system has a single mirror symmetry and the current is applied perpendicular to this mirror plane (as is the case for the MoTe_2/Py interface of Device 1 in

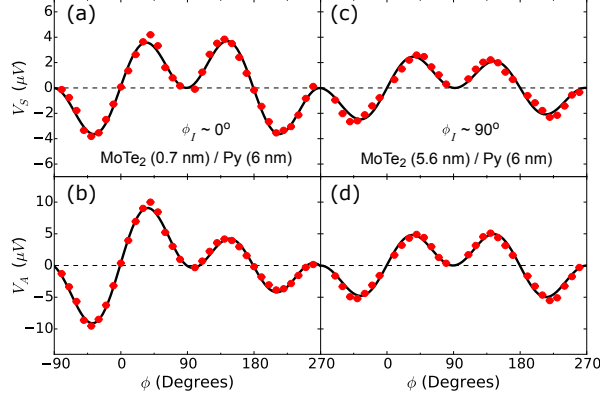


FIG. 2. a and b) Dependence on the applied field angle for both the (a) symmetric, V_S , and (b) antisymmetric, V_A , component of the mixing voltage for Device 1, MoTe₂(monolayer) / Py(6 nm) with current applied perpendicular to the MoTe₂ mirror plane. Fits of the angular dependence are made using Eqs. 3 and 4. An out-of-plane antidamping torque is observed, with fit values $B/A = 0.302 \pm 0.001$. c and d) Dependence on the applied field angle for (c) V_S and (d) V_A in Device 2, MoTe₂(5.6 nm) / Py(6 nm) with current applied along the MoTe₂ mirror plane. No out-of-plane antidamping torque is observed within experimental uncertainty, consistent with the symmetry requirements of the MoTe₂ surface. In both samples the applied microwave power is 5 dBm at 9 GHz.

Fig. 2a,b) a net torque generated by an out-of-plane spin is allowed by symmetry (a torque $\propto \hat{m} \times \hat{z}$ or $\propto \hat{m} \times (\hat{m} \times \hat{z})$). However, if the current instead flows along a mirror plane, such a torque is forbidden by symmetry. Figure 2c and d shows V_S and V_A for a MoTe₂/Py device in which current is applied along the MoTe₂ mirror plane (Device 2). Consistent with this symmetry requirement, fits of V_A using Eq. 3 yield values of B that are zero within experimental uncertainty. We note the presence of a small, but nonzero, value of T as determined by fits of V_S using Eq. 4, $T/S = 0.067 \pm 0.003$, which is discussed below and in Appendix F.

The torque conductivity, defined as the angular momentum absorbed by the magnet per second per unit interface area per unit applied electric field, provides an absolute measure of the torques produced in a spin source/ferromagnet heterostructure nominally independent of geometric factors. For a torque τ_K (where $K = A, B, C, S, T$ or U) we calculate the

corresponding torque conductivity via

$$\sigma_K = \frac{M_s l w t_{\text{Py}}}{\gamma} \frac{\tau_K}{(l w) E} = \frac{M_s l t_{\text{Py}}}{\gamma} \frac{\tau_K}{I_{\text{RF}} \cdot Z_{\text{RF}}}, \quad (5)$$

where M_s is the saturation magnetization, E is the electric field, l and w are the length and width of the MoTe₂/Py bilayer, $t_{\text{Py}} = 6$ nm is the thickness of the Py, and Z_{RF} is the device impedance. The factor $M_s l w t_{\text{Py}}/\gamma$ is the total angular momentum of the magnet, and converts the normalized torque into units of angular momentum per second. Further details of the ST-FMR analysis can be found in Appendix A.

We have determined the torque conductivities for 20 MoTe₂(t_{TMD})/Py(6 nm) devices, all with distinct thicknesses of MoTe₂, t_{TMD} , and angles between the current direction and the MoTe₂ mirror plane. Details of each device can be found in Table I of the Appendix. We define ϕ_I as the angle between the current and the vector normal to the MoTe₂ mirror plane (typically called the b-axis in the β phase), such that $\phi_I = 0^\circ$ is perpendicular to the mirror plane and $\phi_I = 90^\circ$ is parallel. Figure 3a shows σ_B as a function of ϕ_I for 17 of our devices (we have excluded our bilayer thick MoTe₂ devices for now, which will be discussed later). Consistent with the symmetry requirements on the torques, σ_B is largest when current is applied perpendicular to the MoTe₂ mirror plane and is progressively reduced as more of the applied current flows along the mirror plane. Note that in Fig. 3a we have plotted $|\sigma_B|$. This is because the sign of σ_B is not solely determined by ϕ_I but also the canting of the molybdenum dimerization at the MoTe₂/Py interface, which we do not control and cannot determine by polarized Raman spectroscopy (to visualize this difference, consider a two-fold rotation about the MoTe₂ c-axis for a monolayer).

In contrast to the strong dependence on ϕ_I for σ_B , the torque conductivity for the conventional component of in-plane antidamping spin Hall torque, σ_S , shows no significant dependence (Fig. 3b). This is similar to the σ_S dependence on ϕ_I observed in our WTe₂/Py heterostructures[12, 13]. We note, however, that the relative insensitivity of σ_S to the in-plane current direction observed in β -MoTe₂ and WTe₂ is not required by symmetry, and in general the magnitudes of the in-plane spins generated in response to a current along the a or b-axes are allowed to differ[34]. We obtain an average value of σ_S for our MoTe₂/Py devices of $5800 \pm 160 \hbar/(2e)$ ($\Omega^{-1}m^{-1}$), smaller than the average value observed in our WTe₂/Py heterostructures, $8000 \pm 200 \hbar/(2e)$ ($\Omega^{-1}m^{-1}$) [12, 13], and larger than the $\approx 3000 \hbar/(2e)$ ($\Omega^{-1}m^{-1}$) observed in our NbSe₂/Py heterostructures [14].

To help analyze the mechanism that drives the spin-orbit torques in our MoTe₂/Py heterostructures, it is helpful to study the torques as a function of MoTe₂ thickness, holding the crystal alignment fixed. In Appendix D, we discuss the observed thickness dependence for σ_A , and show that this torque contribution is dominated by the Oersted field. Figure 4a shows the thickness dependence for σ_B and σ_S for devices with current aligned perpendicular to the MoTe₂ mirror plane, where $|\phi_I| < 15^\circ$ and usually less than 10° . Both torques are largely independent of MoTe₂ thickness, with the notable exception of bilayer MoTe₂ devices, implying an interfacial origin for these torque components. This is in qualitative similarity to the TMD thickness dependence previously observed in WTe₂. The striking exception in the thickness dependence is from our devices in which the MoTe₂ is just a bilayer (1.4 nm) thick (3 different samples). In these devices, no out-of-plane antidamping torque is observed

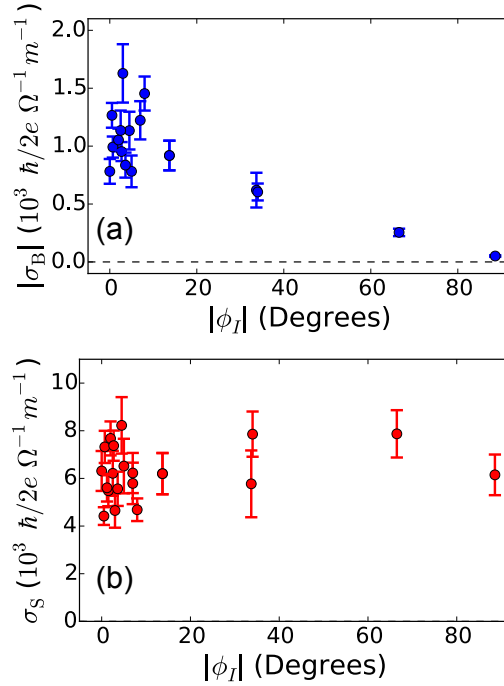


FIG. 3. a) Torque conductivities for the out-of-plane antidamping torque, τ_B , as a function of the angle $|\phi_I|$ for 17 of our MoTe₂/Py devices, all with distinct MoTe₂ thicknesses. We have excluded our bilayer MoTe₂ devices in this plot, which are discussed in detail later. b) Torque conductivities for the standard in-plane antidamping torque, τ_S , as a function of $|\phi_I|$ in all of our MoTe₂/Py devices. In both plots the applied microwave power is 5 dBm. Torque conductivities are averaged over measurements at frequencies 8-11 GHz in steps of 1 GHz.

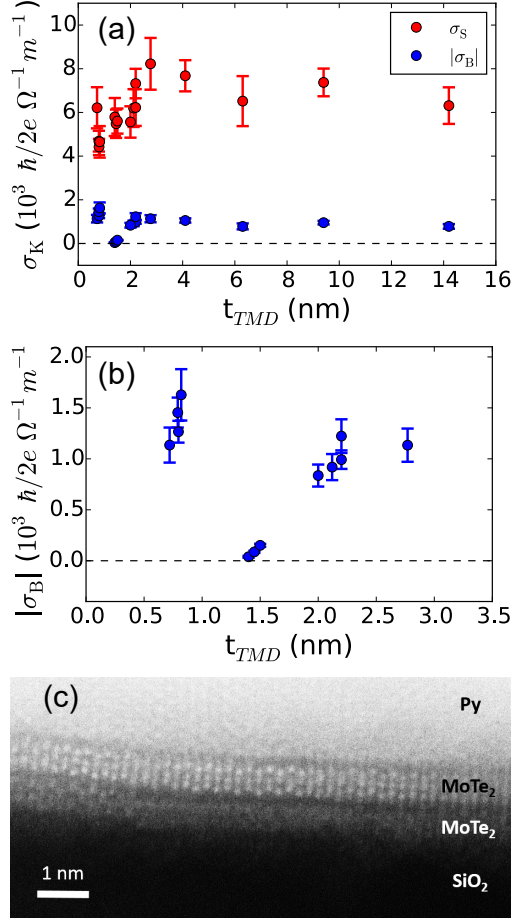


FIG. 4. a) The torque conductivities σ_B and σ_S as a function of TMD thickness for devices with current aligned perpendicular to the MoTe₂ mirror plane. b) Detail of the thickness dependence of σ_B in the monolayer to quadlayer regime (with a layer step size of ~ 0.7 nm). The devices that show a value near zero are bilayer MoTe₂. The applied microwave power is 5 dBm. Torque conductivities are averaged over measurements at frequencies 8-11 GHz in steps of 1 GHz. c) Cross-sectional HAADF-STEM image of a MoTe₂(1.4 nm)/Py device looking down the β -MoTe₂ a-axis and along the b-axis. The image shows two MoTe₂ layers, where the layer interfaced with the Si/SiO₂ substrate (white MoTe₂ label) shows regions of disorder which we attribute to partial oxidation. The Py is polycrystalline.

within our experimental uncertainty. Excluding the bilayer devices, we find an average value for $|\sigma_B| = 1020 \pm 30 \hbar/(2e) (\Omega^{-1} m^{-1})$. It is interesting that while the magnitude of σ_S in MoTe₂ is similar to that observed in our WTe₂ devices, the value of $|\sigma_B|$ is approximately 1/3 that of WTe₂ [12, 13].

Figure 4b shows in more detail the measured out-of-plane antidamping torque conductivity $|\sigma_B|$ in MoTe₂/Py heterostructures in monolayer steps from a single MoTe₂ layer to quadlayer MoTe₂, all with current perpendicular to the MoTe₂ mirror plane. The contrast is striking between the large torques in the monolayer, trilayer and quadlayer MoTe₂ devices, and the nearly-zero torque in the three bilayer samples. In our previous work on WTe₂/Py devices, bilayer WTe₂ (two samples) also showed a decrease in σ_B , although in that case σ_B for the bilayer devices was $\sim 1/2$ that of the monolayer and trilayer devices rather than zero (see Fig. 5 of Ref. [13]). The origin of these reductions is unknown. Only the out-of-plane antidamping torque is reduced, not σ_S or σ_A . In WTe₂, non-symmorphic crystal symmetries (the b-c glide plane and c-axis screw) require that the spin responsible for generating τ_B must have opposite signs in adjacent layers [13]. While β -MoTe₂ does not possess the same non-symmorphic symmetries, there is an effective in-plane polar vector at the β -MoTe₂/Py interface that changes sign for adjacent β -MoTe₂ layers [35], which could lead to oppositely-directed current-induced out-of-plane spins in adjacent layers. Such a layer-dependent sign for the out-of-plane spin might lead to a partial cancellation of contributions from adjacent layers, and may have some bearing on this layer-dependent effect. However, this mechanism alone is difficult to reconcile with our observations that a strong layer dependence is present only in the bilayer MoTe₂, and that the lower layer in our bilayer devices is also likely partially oxidized (see below).

The in-plane field-like torque, $\vec{\tau}_T \propto \hat{m} \times \hat{z}$, has the same symmetry constraints as $\vec{\tau}_B$ and is symmetry allowed in our MoTe₂/Py devices when the current is applied perpendicular to the MoTe₂ mirror plane. Interestingly, we observe significant values of σ_T only in devices with sufficiently thick MoTe₂, above about 3 nm. Details can be found in Appendix F and H. In all such devices the ratio of σ_T/σ_B is always negative, even though the signs of σ_T and σ_B vary from sample to sample. In addition, we find that τ_T and τ_B scale similarly with the sample temperature. These observations suggest that the two torque components are correlated. However, we also find that σ_T and σ_B have distinct dependencies on the MoTe₂ thickness, in tension with the idea that the two torques are generated through the same mechanism. Surprisingly, we also find a significant, though reduced, value of σ_T in samples where current is flowed predominately along the MoTe₂ mirror plane (Fig. 2c) – *i.e.* the condition under which the torque is symmetry forbidden. This suggests the possibility of two distinct mechanisms contributing to the generation of τ_T : one which is correlated with

τ_B and the MoTe₂ crystal structure, and the other independent of the nominal MoTe₂ crystal structure and possibly due to strain induced by the fabrication procedure [14, 36]. We note that the observation of non-zero values of both σ_B and σ_T in the same sample is in contrast to previous measurements on other TMDs. In WTe₂ we did not observe any significant value of τ_T even though a large τ_B was present (see Fig. 6 of Ref. [13]). For (presumably) strained NbSe₂/Py devices the situation was exactly the opposite. There we observed a large value of τ_T , but no τ_B , though with no clear dependence on the TMD thickness.

To better understand the microscopic structure of the MoTe₂/Py samples, we have performed cross-sectional high-angle annular dark-field scanning transmission electron microscopy (HAADF-STEM) imaging on a bilayer β -MoTe₂/Py device (Fig. 4c) as initially identified by AFM. Both β -MoTe₂ layers are clearly visible. However, the layer adjacent to the Si/SiO₂ substrate shows increased localized disorder in some regions, which we attribute to partial oxidation. Note that this partially oxidized layer remains crystallographically oriented in the unoxidized regions, while the top layer appears pristine. Oxidation just of the lower MoTe₂ layer is consistent with our sample fabrication process – the layer of MoTe₂ adjacent to the substrate is exposed to air before being placed on the substrate for exfoliation, while the other layers are protected from air exposure throughout the fabrication process. The existence of partial oxidation of the lowest MoTe₂ layer is also consistent with the signal strengths from our polarized Raman spectroscopy measurements for monolayer and bilayer thick β -MoTe₂/Py devices: the bilayer thick samples show a strong signal, whereas the monolayer devices show a significantly weaker signal, but with no evidence of crystallographic twinning in either data set (see Appendix).

In summary, we have studied the current-induced spin-orbit torques in β -MoTe₂/Py heterostructures at room temperature. We have observed an out-of-plane antidamping torque, τ_B , qualitatively similar to the τ_B observed in WTe₂/Py heterostructures. This torque is consistent with the symmetries of the MoTe₂ surface – at the interface of MoTe₂ and Py the structural symmetries are limited to a single mirror plane, and consistent with that symmetry, τ_B is observed only when a component of the current is applied perpendicular to that mirror plane. This demonstrates that breaking of inversion symmetry in the bulk of the spin-generation layer is not a necessary requirement for τ_B . The magnitude of the observed torque conductivity is $\sim 1/3$ that observed in similar devices that use WTe₂ as the spin source layer. In both materials σ_B is largely independent of the TMD thickness.

The torque conductivity for the standard antidamping torque, σ_S , is also independent of thickness indicating that both torques are likely generated by an interfacial mechanism. The notable exception in the thickness dependence of σ_B is for bilayer-thick MoTe_2 devices, for which σ_B is zero to within measurement uncertainty. Bilayer WTe_2 devices also have a greatly-reduced out-of-plane antidamping torque compared to monolayer or trilayer devices, but the origin of this effect is unknown.

Acknowledgements: GMS acknowledges useful conversations with Dr. David MacNeill. The primary support for this project came from the US Department of Energy (de-sc0017671). Electron microscopy was performed with support from the NSF through PARADIM as part of the Materials for Innovation Platform Program. Sample fabrication was performed in the shared facilities of the Cornell Center for Materials Research (NSF DMR-1719875) and at the Cornell Nanoscale Science & Technology Facility, part of the National Nanotechnology Coordinated Infrastructure, which is supported by the NSF (NNCI-1542081). The FEI Titan Themis 300 was acquired through Grant NSF-MRI-1429155, with additional support from Cornell University, the Weill Institute, and the Kavli Institute at Cornell.

Appendix A: Calibrated ST-FMR measurements

To make a quantitative measurement of the magnitude of the torques using Eqs. 1 and 2 we must first determine values for α_G , $R(\phi)$, and I_{RF} . The Gilbert damping is estimated from the frequency dependence of the linewidth via $\Delta = 2\pi f\alpha_G/\gamma + \Delta_0$, where Δ_0 is the inhomogeneous broadening. $R(\phi)$ is determined by measurements of the device resistance as a function applied in-plane magnetic field angle (with a field magnitude of 0.1 T). The RF current is determined by calibrating the reflection coefficients of our devices (S_{11}) and the transmission coefficient of our RF circuit (S_{21}) through vector network analyzer measurements. These calibrations allow calculation of the RF current flowing in the device as a function of applied microwave power and frequency:

$$I_{\text{RF}} = 2\sqrt{1\text{mW} \cdot 10^{\frac{P_s(\text{dBm}) + S_{21}(\text{dBm})}{10}} (1 - |\Gamma|)^2 / 50\Omega} \quad (\text{A1})$$

where P_s is the power sourced by the microwave generator and $\Gamma = 10^{S_{11}(\text{dBm})/20}$. The frequency dependent device impedance, Z_{RF} , is given by $50\Omega \cdot (1 + \Gamma)/(1 - \Gamma)$.

Device	t (nm)	$L \times W$ (μm)	σ_S	σ_B	σ_T	$ \phi_I $ (degrees)
Number	± 0.3 nm	± 0.2 μm	$(10^3 \hbar/2e \Omega^{-1}m^{-1})$	$(10^3 \hbar/2e \Omega^{-1}m^{-1})$	$(10^3 \hbar/2e \Omega^{-1}m^{-1})$	$\pm 5^\circ$
1	0.7	5×4	-6.2(1)	-1.1(2)	0.026(5)	3
2	5.6	5×4	-6.1(9)	0.051(7)	-0.39(6)	89
3	6.3	5×4	-7(1)	-0.8(1)	0.8(1)	5
4	1.4	5×4	-5.8(9)	-0.04(1)	-0.22(5)	7
5	14.2	5×4	-6.3(8)	-0.8(1)	0.7(1)	0
6	2.1	5×4	-6.2(9)	0.9(1)	-0.13(2)	14
7	2.2	5×4	-7.3(7)	-0.99(9)	0.032(5)	1
8	2.8	5×4	-8(1)	-1.1(2)	0.28(4)	5
9	4.1	5×4	-7.7(7)	1.1(1)	-0.78(7)	2
10	9.4	5×4	-7.4(6)	0.95(8)	-1.0(1)	3
11	0.8	5×4	-4.4(4)	-1.3(1)	0.14(1)	1
12	1.5	5×4	-5.5(7)	-0.09(1)	0.25(3)	2
13	1.5	5×4	-5.6(6)	-0.15(2)	0.23(2)	1
14	2.0	5×4	-5.6(7)	-0.8(1)	0.21(3)	4
15	2.2	5×4	-6.2(8)	1.2(2)	0.18(2)	7
16	0.8	5×4	-4.7(5)	-1.4(1)	0.06(1)	8
17	0.8	5×4	-4.7(7)	1.6(3)	0.08(1)	3
18	2.2	5×4	-5(1)	0.6(2)	-0.17(4)	34
19	2.3	4.5×4	-8(1)	-0.60(7)	-0.41(5)	34
20	9.4	4×3	-8(1)	-0.26(3)	-0.55(7)	67

TABLE I. Comparison of device parameters, and torque conductivities for MoTe₂/Py bilayers. Here ϕ_I is the angle between the current and the crystal axis perpendicular to the MoTe₂ mirror plane as measured by polarized Raman spectroscopy. For the torque conductivities, the () gives the uncertainty of the last reported digit.

In order to determine a torque conductivity (Eq. 5), we must also obtain a value of M_s for the Py. As M_s is influenced by the material on which the Py grows (here, MoTe₂), and as mm-scale β -MoTe₂/Permalloy heterostructures are unavailable, we are unable to measure M_s directly via magnetometry. Instead we approximate $M_s \approx M_{\text{eff}}$, which we have found to be accurate in other Py heterostructure systems. We estimate an average value of $\mu_o M_{\text{eff}} = 0.84 \pm 0.01$ T as extracted from the ST-FMR measurements.

Appendix B: Devices Parameters

Table I shows a comparison of device parameters and torque conductivities for all samples presented in this work.

Appendix C: Determination of Crystal Orientation

Crystals of β -MoTe₂ exfoliate in the a-b plane and are generally elongated in the Mo-chain direction, with sharp and cleanly cleaved edges running parallel to that direction. This is very similar to WTe₂, and can be used as a first-order approximation of the in-plane crystal axis during device fabrication. We have also verified the crystal orientation more precisely for each of our devices using Raman spectroscopy.

1. Raman Spectroscopy

The Raman spectra of MoTe₂ has been well characterized in all three crystal phases [26–32]. We performed Raman measurements with a confocal Raman microscope using a linearly polarized 488 nm excitation and a parallel polarizer placed in front of the spectrometer. The sample is aligned to the linear polarization direction (along the length of the device) and spectra are taken as the sample is rotated in steps of 10°. The maximum of the ~ 133 cm⁻¹ and ~ 250 cm⁻¹ peaks correspond to the MoTe₂ b-axis. Figure 5 shows polarized Raman spectra for two MoTe₂/Py devices in which the MoTe₂ is (a,b) a monolayer and (c,d) a bilayer thick. The symmetries of the observed peaks are consistent with previous measurements [26, 27]. No evidence of crystallographic twinning is observed in the polarized Raman spectra.

2. Magnetic Easy Axis

In WTe₂/Py bilayers, we observed previously that the WTe₂ induced a strong in-plane magnetic easy axis that corresponded with the b-axis of the crystal, regardless of the applied current direction [12, 13]. This correlation provided an efficient means for extracting the angle between the WTe₂ crystal axes and the current direction through electrical measurements alone. However, we find that MoTe₂ does not induce any significant magnetic

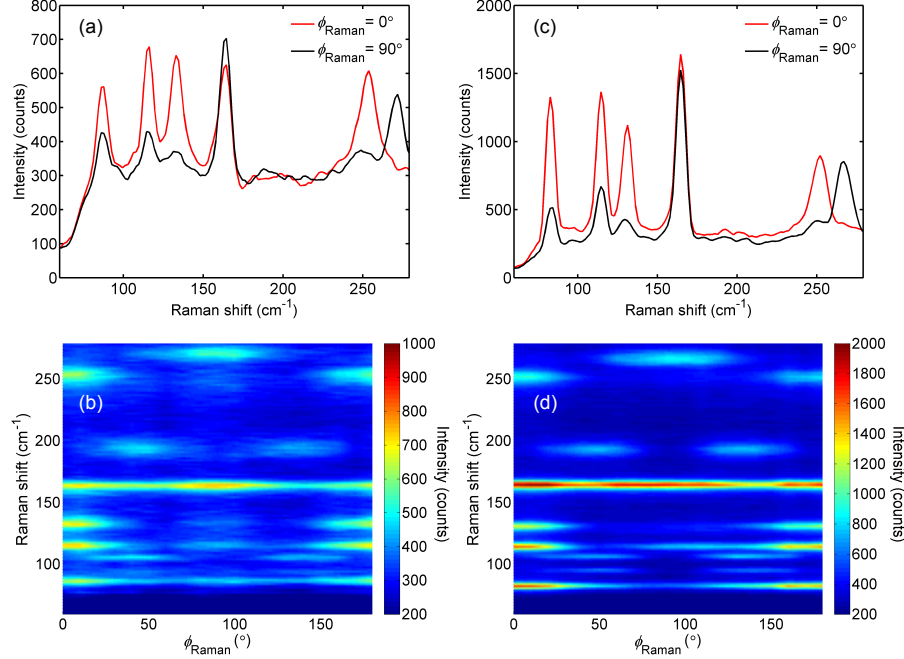


FIG. 5. a,c) Raman spectra for MoTe₂ monolayer and bilayer / Py devices respectively, with a linearly polarized 488 nm excitation aligned parallel to a polarizer in front of the spectrometer. ϕ_{Raman} is the angle between the excitation polarization and the device current direction (along the bar). The red traces show spectra with the polarization parallel to the current and the black traces show spectra with the polarization perpendicular. b,d) Angular dependence of the Raman spectra for the two devices. The color map represents the peak intensity (with units of counts), where both spectra are taken under the same excitation power. The maximum of the $\sim 133 \text{ cm}^{-1}$ and $\sim 250 \text{ cm}^{-1}$ peaks correspond to the MoTe₂ b-axis, where $\phi_{\text{Raman}} \rightarrow -\phi_I$.

easy-axis within the Py, so this method cannot be used to characterize the crystal alignment of MoTe₂. TaTe₂ generates a magnetic easy axis with strength intermediate between WTe₂ and MoTe₂ [16]. This variation suggests different degrees of coupling between the TMDs and Permalloy.

Appendix D: Out-Of-Plane Field-Like Torque and Oersted Torque

We extract the individual resistivities of the MoTe₂ and Py layers using the two-point resistances of our devices for which the current is aligned perpendicular to the MoTe₂ mirror plane (*i.e.*, $\phi_I = 0^\circ$) within 15° and usually within 10° , where we have used only devices in

which the Py thin-film and Al capping layers were grown in the same sputtering deposition batch in order to minimize effects from small variations in the Py and Al thicknesses. We plot the inverse of the sheet resistance as a function of t_{TMD} (Fig. 6a), and using the relation:

$$\frac{1}{R_{\square}} = \frac{l}{wR} = \frac{t_{\text{Py}}}{\rho_{\text{Py}}} + \frac{t_{\text{TMD}}}{\rho_{\text{TMD}}}, \quad (\text{D1})$$

extract the resistivities $\rho_{\text{Py}} = 95 \pm 2 \text{ } (\mu\Omega \text{ cm})$ and $\rho_{\text{TMD}} = 550 \pm 75 \text{ } (\mu\Omega \text{ cm})$. The value obtained for ρ_{Py} is similar to that seen in our WTe_2/Py devices when the Py is deposited using glancing-angle sputtering.

Figure 6b shows σ_{A} as a function of t_{TMD} (red circles) for devices in which current is aligned perpendicular to the MoTe_2 mirror plane. A strong thickness dependence of the torques is observed. In many material systems this component of torque, $\propto \hat{m} \times \hat{y}$ (for current in the \hat{x} direction), is dominated by the Oersted torque – that is, the magnetic

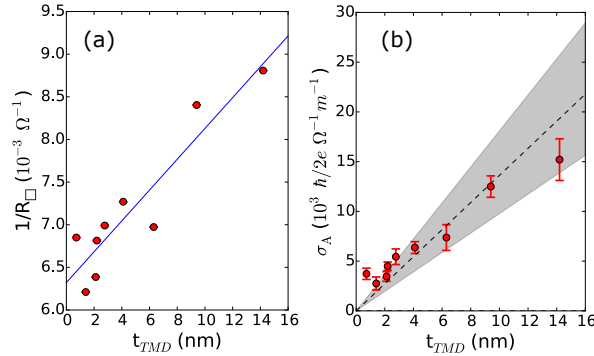


FIG. 6. a) Inverse sheet resistance of devices with current perpendicular to the MoTe_2 mirror plane (red circles) as a function of MoTe_2 thickness as measured by a two-point method. The blue line gives a fit using Eq. D1 to extract the sheet resistances for the Py and MoTe_2 . b) Torque conductivity for the out-of-plane field like torque ($\propto \hat{m} \times \hat{y}$) as a function of thickness for devices with current perpendicular to the MoTe_2 mirror plane (red circles). The dashed line gives the predicted Oersted field contribution from the torques (Eq. D2) and the shaded region gives the spread in the expected contribution as given by the uncertainty in the measured charge conductivity of MoTe_2 . The applied microwave power is 5 dBm. Torque conductivities are averaged over measurements at frequencies 8-11 GHz in steps of 1 GHz. In both plots, we have used only devices in which the Py thin-film and Al capping layers were grown in the same sputtering deposition batch in order to minimize effects from small variations in the Py and Al thicknesses.

field generated from a simple current-carrying wire. For instance, we have previously shown that this is the case in the WTe_2/Py and NbSe_2/Py systems. We can model the torque conductivity generated by the Oersted torque as:

$$\sigma_{\text{Oe}} = \frac{e\mu_0 M_S t_{\text{Py}} \sigma_{\text{TMD}}}{\hbar} t_{\text{TMD}}, \quad (\text{D2})$$

where σ_{TMD} is the charge conductivity of the MoTe_2 . The dashed line in Fig. 6b shows the predicted Oersted torque using the extracted value of ρ_{TMD} and the shaded region about the dashed line gives the uncertainty in the predicted torque as given by the spread in ρ_{TMD} . All devices with the possible exception of our monolayer device are well described by the predicted Oersted torque. Deviation from the predicted Oersted torque in our monolayer device may suggest a non-uniform current distribution in the Py film, as cross-sectional HAADF STEM imaging of one of our $\beta\text{-MoTe}_2$ devices suggests that partial oxidation of the monolayer may play a role in an increased resistivity of that layer, and could affect the growth of the Py on top of such a layer (see Fig. 4c and associated discussion).

Appendix E: Dresselhaus-like Torques

Figure 7 shows the torque conductivities for the torque components $\sigma_C \propto \hat{m} \times \hat{x}$, and $\sigma_U \propto \hat{m} \times (\hat{m} \times \hat{x})$ as a function of applied current direction, ϕ_I . (Recall that $\phi_I = 0^\circ$ corresponds to current directed perpendicular to the MoTe_2 mirror plane.) We refer to the torques σ_C and σ_U as Dresselhaus-like [16]. Symmetry requires that the Dresselhaus-like torques be zero when the current is either along or perpendicular to a mirror plane (*e.g.*, $\phi_I = 0^\circ$ or 90° , the situations for the majority of the samples studied in this work, including all the samples shown in Fig. 4). Consistent with this requirement, in Fig. 7 both σ_C and σ_U are zero when $\phi_I = 0^\circ$ or 90° , and can be nonzero at intermediary angles. At present, we do not have enough devices at intermediary values of ϕ_I to accurately gauge the magnitude of these effects. However, these torque components should arise naturally in $\text{MoTe}_2/\text{ferromagnet}$ heterostructures because MoTe_2 has an in-plane resistivity anisotropy [37], and this will cause spatially non-uniform current flows with non-zero transverse components whenever the voltage is applied at an angle tilted away from a symmetry axis [16].

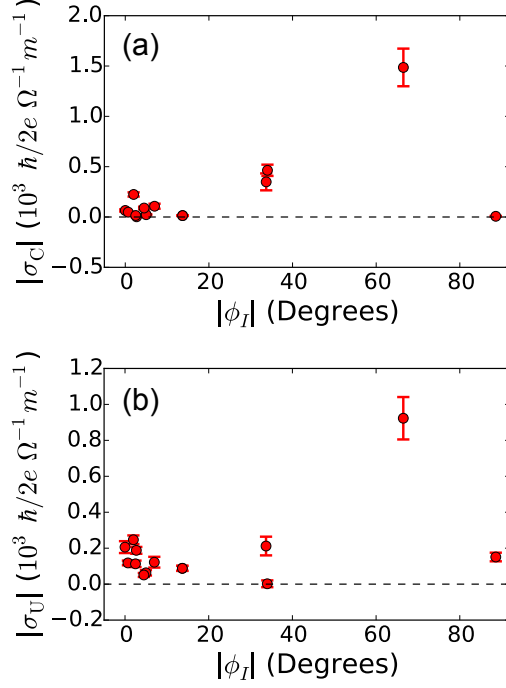


FIG. 7. a and b) Torque conductivities for the Dresselhaus-like torques (a) $\propto \hat{m} \times \hat{x}$ and (b) $\propto \hat{m} \times (\hat{m} \times \hat{x})$ as a function of $|\phi_I|$ for all of our ST-FMR devices. The applied microwave power is 5 dBm. Torque conductivities are averaged over measurements at frequencies 8-11 GHz in steps of 1 GHz.

Appendix F: In-plane Field-like Torque

The symmetry requirements for the in-plane field-like torque component, $\vec{\tau}_T \propto \hat{m} \times \hat{z}$ are identical to that of $\vec{\tau}_B \propto \hat{m} \times (\hat{m} \times \hat{z})$. That is, τ_T is allowed by symmetry if there is a component of current perpendicular to the single mirror plane. In some but not all of our MoTe₂/Py devices we observe a small but nonzero value of τ_T . Figure 8 shows V_S and V_A for one such device (Device 3, with 6.3 nm of MoTe₂) for which current is applied perpendicular to the mirror plane. Fitting V_A and V_S with Eqs. 3 and 4 we can extract a ratio of the torques $\tau_T/\tau_S = -0.114 \pm 0.002$ and $\tau_T/\tau_B = -0.90 \pm 0.02$. We observe significant values of σ_T only in devices with sufficiently thick MoTe₂, above about 3 nm (Fig. 9). The average value of $|\sigma_T|$ for samples with the MoTe₂ thickness greater than 3 nm and $\phi_I \approx 0^\circ$ is $810 \pm 50 \hbar/(2e) (\Omega^{-1} m^{-1})$. In all such devices with the current perpendicular to the mirror plane the ratio of σ_T/σ_B is always negative, even though the signs of σ_T and σ_B vary from sample to sample (see Fig. 9a). This, together with a similar dependence on sample temperature

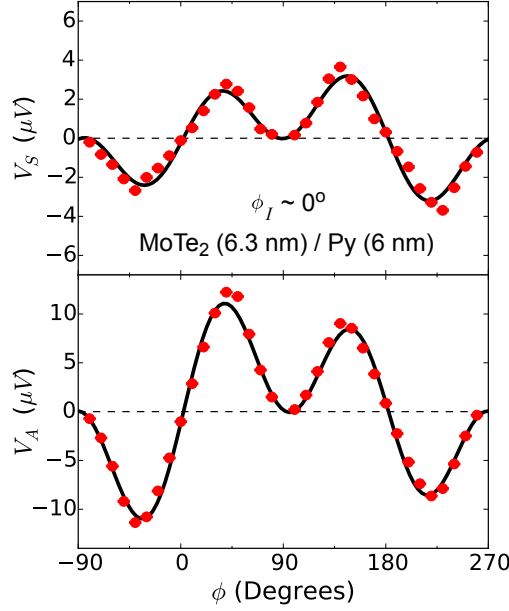


FIG. 8. Dependence on the applied magnetic field angle for both the symmetric, V_S , and antisymmetric, V_A , component of the mixing voltage for a device that shows an in-plane field-like torque $\propto \hat{m} \times \hat{z}$ (Device 3), with MoTe₂(6.3 nm) / Py(6 nm) and current applied perpendicular to the MoTe₂ mirror plane. Fits of the angular dependence are made using Eqs. 3 and 4. The applied microwave power is 5 dBm at 9 GHz

for τ_T and τ_B as discussed in Appendix H, suggests that these two torque components are correlated. We note, however, that σ_T and σ_B exhibit very different thickness dependencies, with σ_T showing a dependence on thickness typically associated with bulk spin-orbit torque generation, whereas σ_B is interfacial in nature.

Figure 9c shows $|\sigma_T|$ as a function of $|\phi_I|$ for devices with TMD thickness above 3 nm. σ_T shows a clear decrease in magnitude as the direction of the current is increasingly aligned along the MoTe₂ mirror plane. However, near $|\phi_I| = 90^\circ$ there remains a significantly non-zero value of σ_T inconsistent with a symmetry analysis of the nominal MoTe₂/Py structure. This is reminiscent of the observed σ_T in NbSe₂/Py devices [14], in which we presumed a uniaxial strain induced by the fabrication procedure reduced the nominally high symmetry NbSe₂ structure in such a way that this torque could be generated [36]. Note that for (presumably) strained NbSe₂/Py devices we observed a large value of τ_T , but no τ_B .

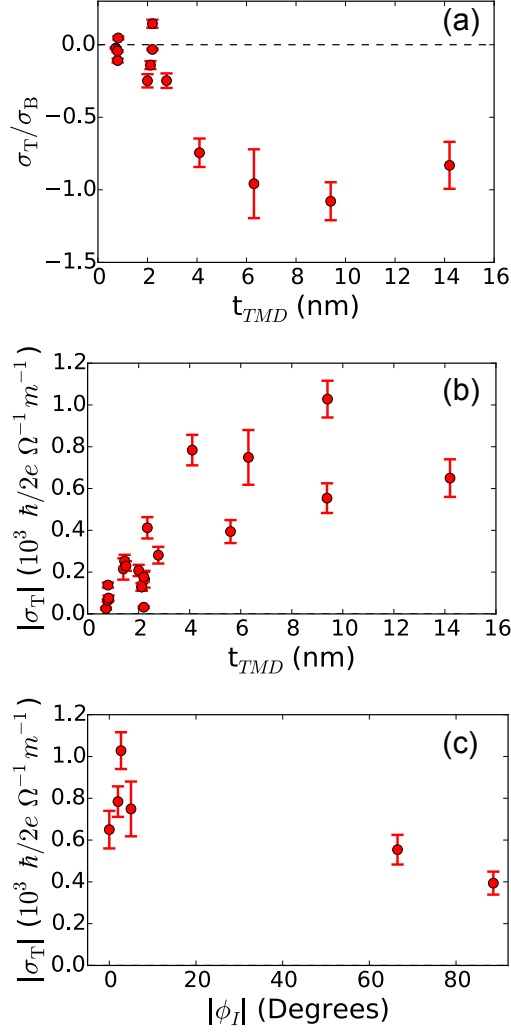


FIG. 9. a) The torque ratio σ_T/σ_B as a function of thickness for devices with the current applied perpendicular to the MoTe_2 mirror plane direction. Note that the ratio is always negative when non-zero. We have excluded the bilayer devices as $\sigma_B \sim 0$. b) Torque conductivity $|\sigma_T|$ as a function of TMD thickness for all devices. The torque is only appreciable above a TMD thickness of 3 nm. c) $|\sigma_T|$ as a function of $|\phi_I|$ for devices with TMD thickness above 3 nm. The applied microwave power is 5 dBm. Torque conductivities are averaged over measurements at frequencies 8-11 GHz in steps of 1 GHz.

Together, these observations suggest that there may be two mechanisms that contribution to σ_T in $\beta\text{-MoTe}_2$: one that is correlated with σ_B and dependent on the MoTe_2 crystal structure, and another that is generated by a symmetry breaking associated with the strain induced during the fabrication procedure.

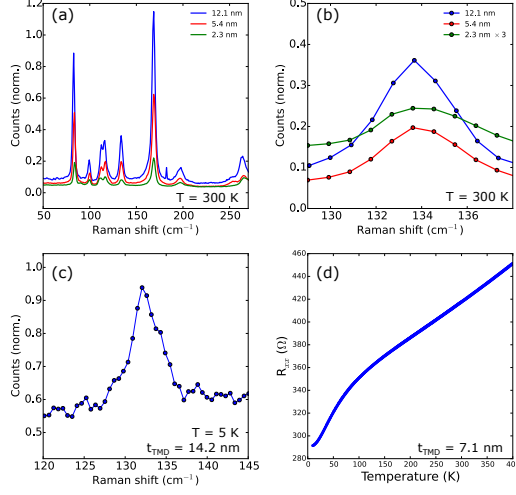


FIG. 10. (a) Raman spectroscopy measurements of MoTe₂/Py samples with the excitation and collection linearly polarized in a parallel configuration along the Mo chain for three different thicknesses at room temperature. (b) A detailed view of the 133 cm⁻¹ mode shown in (a). No peak splitting is observed indicating that the MoTe₂ is in the β phase. Spectra for (a) and (b) are taken with a 532 nm excitation. (c) Raman spectrum with a 633 nm excitation at 5 K for a 14.2 nm MoTe₂/Py device. (d) Four-point resistance of a MoTe₂(7.1 nm)/Py device as a function of temperature, with a sample width of 4 μ m, length 15 μ m and a DC current of 50 μ A.

Appendix G: Determining the Crystal Phase in the Few-Layer Limit

In bulk crystals, MoTe₂ undergoes a hysteretic transition from the β phase to the γ phase when cooled below approximately 250 K [25], with a temperature hysteresis of about 20 K. The orthorhombic (γ) phase is obtained by a shift in the stacking of the van der Waals layers in β -MoTe₂. This phase is isostructural to WTe₂. Both pressure [38, 39] and impurity doping [40–42] have been shown to influence the transition temperature. While the majority of published studies on γ -MoTe₂ have focused on bulk crystals [25, 27, 29, 43–46], a handful of reports have studied the phase transition in thin films [26–28, 32, 47]. Recent work has suggested there may be a thickness dependence to the transition in the few-layer limit [32, 47].

The β and γ phase can be distinguished experimentally through polarized Raman spectroscopy by the presence in the γ phase of one additional peak at ~ 11 cm⁻¹ and a peak splitting in the ~ 133 cm⁻¹ mode [27, 29]. To verify the MoTe₂ crystal phase of our devices,

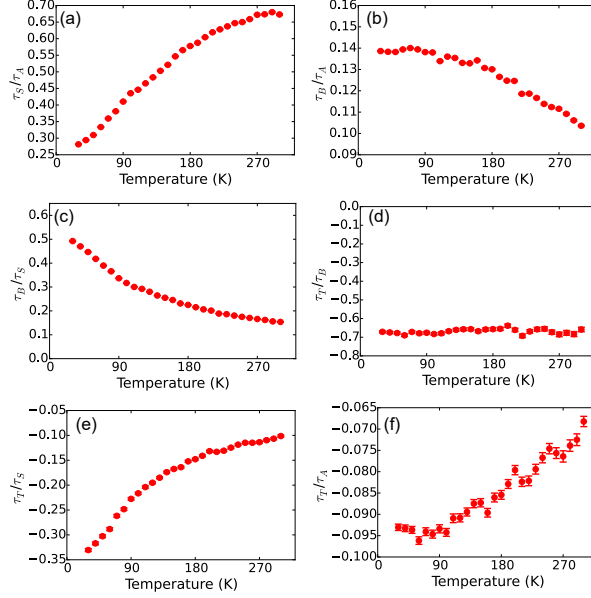


FIG. 11. a-e) Torque ratios as a function of temperature for a MoTe₂(8.6 nm)/Py device with length 4 μm and width 3 μm , with the current applied perpendicular to the MoTe₂ mirror plane ($\phi_I \sim 0^\circ$). The applied microwave power is 8 dBm at a frequency of 9 GHz.

we performed Raman spectroscopy measurements of our MoTe₂/Py films using 532 nm and 633 nm excitations at room temperature and at 5 K (Fig. 10a-c). We see no evidence of the 133 cm^{-1} peak splitting at room temperature for samples with MoTe₂ thicknesses from 2.3 nm to 12.1 nm (Fig. 10b), indicating that at room temperature our films are in the β phase as expected. The 133 cm^{-1} peak splitting in the γ phase is approximately 5 cm^{-1} wide, and so should be resolved by these measurements. The Raman measurements at 5 K also do not show a splitting in the 133 cm^{-1} peak (Fig. 10c). Furthermore, measurements of the four-point resistance of a MoTe₂/Py device as a function of temperature (Fig. 10d) do not show the hysteretic resistivity feature associated with the transition in bulk samples. These data therefore suggest that our thin films are stabilized in the β phase, perhaps due to the deposition of the Py, with no transition to the γ phase in the measured temperature range.

Appendix H: Temperature Dependent Measurements of Spin-Orbit Torque

One of our original motivations for studying spin-orbit torques generated by MoTe₂ was to try to observe changes in the torques as the MoTe₂ underwent a phase transition from

the β to the γ phase as a function of decreasing temperature. As noted in the previous section, it turns out that our device structure stabilizes the β phase so that we did not observe any transition to the γ phase. Consistent with the lack of a phase transition in the Raman and four-point resistivity data, measurements of the spin-orbit torques as a function of temperature also reveal a smooth evolution, with no indication of an abrupt transition.

We performed temperature-dependent ST-FMR measurements for one of our MoTe₂/Py devices ($t_{\text{TMD}} = 8.6$ nm, length $4\text{ }\mu\text{m}$ and width $3\text{ }\mu\text{m}$), where current is applied perpendicular to the MoTe₂ mirror plane ($\phi_I \sim 0^\circ$). Figure 11 shows the ratios of the measured torques as a function of temperature, where the torque magnitudes are extracted from the angular dependence of the applied field direction for V_A and V_S , as discussed in the main text. The reason why we plot torque ratios rather than individual values is that it is difficult to calibrate accurately within our cryostat the exact value of the microwave current within the sample. We observe a smooth increase in the Oersted torque τ_A with decreasing temperature, reflected in a decrease in the ratio τ_S/τ_A . This is consistent with the decrease in resistivity of MoTe₂ as a function of decreasing temperature, but with no indication of a phase transition to the γ phase. The out-of-plane antidamping component τ_B increases as temperature decreases while the corresponding in-plane antidamping component τ_S decreases, meaning that the total effective tilt angle of the generated antidamping torque is increasingly pulled out of plane with decreasing temperature. The ratio of τ_T/τ_B is constant, indicating that the two torques have the same dependence on temperature. This is additional evidence for the conjecture that these two torque components may arise from related microscopic mechanisms (see discussion in Appendix F).

-
- [1] A. Brataas, A. D. Kent, and H. Ohno, *Nature Materials* **11**, 372 (2012).
 - [2] I. M. Miron, G. Gaudin, S. Auffret, B. Rodmacq, A. Schuhl, S. Pizzini, J. Vogel, and P. Gambardella, *Nature materials* **9**, 230 (2010).
 - [3] I. M. Miron, K. Garello, G. Gaudin, P.-J. Zermatten, M. V. Costache, S. Auffret, S. Bandiera, B. Rodmacq, A. Schuhl, and P. Gambardella, *Nature* **476**, 189 (2011).
 - [4] L. Liu, T. Moriyama, D. C. Ralph, and R. A. Buhrman, *Physical Review Letters* **106**, 036601 (2011).

- [5] L. Liu, O. J. Lee, T. J. Gudmundsen, D. C. Ralph, and R. A. Buhrman, *Phys. Rev. Lett.* **109**, 096602 (2012).
- [6] L. Liu, C.-F. Pai, Y. Li, H. W. Tseng, D. C. Ralph, and R. A. Buhrman, *Science* **336**, 555 (2012).
- [7] C. F. Pai, L. Liu, Y. Li, H. W. Tseng, D. C. Ralph, and R. A. Buhrman, *Applied Physics Letters* **101**, 122404 (2012).
- [8] A. R. Mellnik, J. S. Lee, A. Richardella, J. L. Grab, P. J. Mintun, M. H. Fischer, A. Vaezi, A. Manchon, E.-A. Kim, N. Samarth, and D. C. Ralph, *Nature* **511**, 449 (2014).
- [9] Y. Fan, P. Upadhyaya, X. Kou, M. Lang, S. Takei, Z. Wang, J. Tang, L. He, L.-T. Chang, M. Montazeri, G. Yu, W. Jiang, T. Nie, R. N. Schwartz, Y. Tserkovnyak, and K. L. Wang, *Nature Materials* **13**, 699 (2014).
- [10] W. Zhang, J. Sklenar, B. Hsu, W. Jiang, M. B. Jungfleisch, J. Xiao, F. Y. Fradin, Y. Liu, J. E. Pearson, J. B. Ketterson, Z. Yang, and A. Hoffmann, *APL Materials* **4**, 032302 (2016).
- [11] Q. Shao, G. Yu, Y. W. Lan, Y. Shi, M. Y. Li, C. Zheng, X. Zhu, L. J. Li, P. K. Amiri, and K. L. Wang, *Nano Letters* **16**, 7514 (2016).
- [12] D. MacNeill, G. M. Stiehl, M. H. D. Guimarães, R. A. Buhrman, J. Park, and D. C. Ralph, *Nature Physics* **13**, 300 (2017).
- [13] D. MacNeill, G. M. Stiehl, M. H. D. Guimarães, N. D. Reynolds, R. A. Buhrman, and D. C. Ralph, *Physical Review B* **96**, 054450 (2017).
- [14] M. H. D. Guimarães, G. M. Stiehl, D. MacNeill, N. D. Reynolds, and D. C. Ralph, *Nano Lett.* **18**, 1311 (2018).
- [15] P. Li, W. Wu, Y. Wen, C. Zhang, J. Zhang, S. Zhang, Z. Yu, S. A. Yang, A. Manchon, and X.-X. Zhang, *Nature Communications* **9**, 3990 (2018).
- [16] G. M. Stiehl, D. MacNeill, N. Sivadas, I. El Baggari, M. H. D. Guimarães, N. D. Reynolds, L. F. Kourkoutis, C. Fennie, R. A. Buhrman, and D. C. Ralph, *ACS Nano* **13**, 2599 (2019).
- [17] S.-H. C. Baek, V. P. Amin, Y.-W. Oh, G. Go, S.-J. Lee, G.-H. Lee, K.-J. Kim, M. D. Stiles, B.-G. Park, and K.-J. Lee, *Nature Materials* **17**, 509 (2018).
- [18] C. Safranski, E. A. Montoya, and I. N. Krivorotov, *Nature Nanotechnology* (2018).
- [19] J. D. Gibbons, D. MacNeill, R. A. Buhrman, and D. C. Ralph, *Phys. Rev. Applied* **9**, 064033 (2018).
- [20] Y. Ou, Z. Wang, C. S. Chang, H. P. Nair, H. Paik, N. Reynolds, D. C. Ralph, D. A. Muller,

- D. G. Schlom, and R. A. Buhrman, ArXiv:1810.11136 (2018).
- [21] D. Fang, H. Kurebayashi, J. Wunderlich, K. Výborný, L. P. Zârbo, R. P. Campion, A. Casiraghi, B. L. Gallagher, T. Jungwirth, and A. J. Ferguson, *Nature Nanotechnology* **6**, 413 (2011).
 - [22] H. Kurebayashi, J. Sinova, D. Fang, A. C. Irvine, T. D. Skinner, J. Wunderlich, V. Novák, R. P. Campion, B. L. Gallagher, E. K. Vehstedt, L. P. Zârbo, K. Výborný, A. J. Ferguson, and T. Jungwirth, *Nature Nanotechnology* **9**, 211 (2014).
 - [23] T. D. Skinner, K. Olejník, L. K. Cunningham, H. Kurebayashi, R. P. Campion, B. L. Gallagher, T. Jungwirth, and A. J. Ferguson, *Nature Communications* **6**, 6730 (2015).
 - [24] C. Ciccarelli, L. Anderson, V. Tshitoyan, A. J. Ferguson, F. Gerhard, C. Gould, L. W. Molenkamp, J. Gayles, J. Železný, L. Šmejkal, Z. Yuan, J. Sinova, F. Freimuth, and T. Jungwirth, *Nature Physics* **12**, 855 (2016).
 - [25] R. Clarke, E. Marseglia, and H. P. Hughes, *Philosophical Magazine B* **38**, 121 (1978).
 - [26] R. Beams, L. G. Canado, S. Krylyuk, I. Kalish, B. Kalanyan, A. K. Singh, K. Choudhary, A. Bruma, P. M. Vora, F. Tavazza, A. V. Davydov, and S. J. Stranick, *ACS Nano* **10**, 9626 (2016).
 - [27] S.-Y. Chen, T. Goldstein, D. Venkataraman, A. Ramasubramaniam, and J. Yan, *Nano Letters* **16**, 5852 (2016).
 - [28] L. Zhou, S. Huang, Y. Tatsumi, L. Wu, H. Guo, Y.-Q. Bie, K. Ueno, T. Yang, Y. Zhu, J. Kong, R. Saito, and M. Dresselhaus, *Journal of the American Chemical Society* **139**, 8396 (2017).
 - [29] K. Zhang, C. Bao, Q. Gu, X. Ren, H. Zhang, K. Deng, Y. Wu, Y. Li, J. Feng, and S. Zhou, *Nature Communications* **7**, 13552 (2016).
 - [30] Y. Wang, J. Xiao, H. Zhu, Y. Li, Y. Alsaid, K. Yan Fong, Y. Zhou, S. Wang, W. Shi, Y. Wang, A. Zettl, E. Reed, and X. Zhang, *Nature* **550** (2017).
 - [31] S. Cho, S. Kim, J. H. Kim, J. Zhao, J. Seok, D. H. Keum, J. Baik, D.-H. Choe, K. J. Chang, K. Suenaga, S. W. Kim, Y. H. Lee, and H. Yang, *Science* **349**, 625 (2015).
 - [32] R. He, S. Zhong, H. H. Kim, G. Ye, Z. Ye, L. Winford, D. McHaffie, I. Rilak, F. Chen, X. Luo, Y. Sun, and A. W. Tsen, *Phys. Rev. B* **97**, 041410(R) (2018).
 - [33] K. Garelo, I. M. Miron, C. O. Avci, F. Freimuth, Y. Mokrousov, S. Blügel, S. Auffret, O. Boulle, G. Gaudin, and P. Gambardella, *Nature Nanotechnology* **8**, 587 (2013).
 - [34] L. J. Zhu, D. C. Ralph, and R. A. Buhrman, *Phys. Rev. B* **98**, 134406 (2018).

- [35] L.-K. Shi and J. C. W. Song, Phys. Rev. B **99**, 035403 (2019).
- [36] J. Lee, Z. Wang, H. Xie, K. F. Mak, and J. Shan, Nature Materials **16**, 887 (2017).
- [37] H. P. Hughes and R. H. Friend, Journal of Physics C: Solid State Physics **11**, L103 (1978).
- [38] Y. Qi, P. G. Naumov, M. N. Ali, C. R. Rajamathi, W. Schnelle, O. Barkalov, M. Hanfland, S.-C. Wu, C. Shekhar, Y. Sun, V. Süß, M. Schmidt, U. Schwarz, E. Pippel, P. Werner, R. Hillebrand, T. Förster, E. Kampert, S. Parkin, R. J. Cava, C. Felser, B. Yan, and S. A. Medvedev, Nature Communications **7**, 11038 (2016).
- [39] C. Heikes, I.-L. Liu, T. Metz, C. Eckberg, P. Neves, Y. Wu, L. Hung, P. Piccoli, H. Cao, J. Leao, J. Paglione, T. Yildirim, N. P. Butch, and W. Ratcliff, Phys. Rev. Materials **2**, 074202 (2018).
- [40] D. Rhodes, D. A. Chenet, B. E. Janicek, C. Nyby, Y. Lin, W. Jin, D. Edelberg, E. Mannebach, N. Finney, A. Antony, T. Schiros, T. Klarr, A. Mazzoni, M. Chin, Y. c. Chiu, W. Zheng, Q. R. Zhang, F. Ernst, J. I. Dadap, X. Tong, J. Ma, R. Lou, S. Wang, T. Qian, H. Ding, R. M. Osgood, D. W. Paley, A. M. Lindenberg, P. Y. Huang, A. N. Pasupathy, M. Dubey, J. Hone, and L. Balicas, Nano Letters **17**, 1616 (2017).
- [41] S. M. Oliver, R. Beams, S. Krylyuk, I. Kalish, A. K. Singh, A. Bruma, F. Tavazza, J. Joshi, I. R. Stone, S. J. Stranick, A. V. Davydov, and P. M. Vora, 2D Materials **4**, 045008 (2017).
- [42] H.-J. Kim, S.-H. Kang, I. Hamada, and Y.-W. Son, Phys. Rev. B **95**, 180101(R) (2017).
- [43] A. Tamai, Q. S. Wu, I. Cucchi, F. Y. Bruno, S. Riccò, T. K. Kim, M. Hoesch, C. Barreteau, E. Giannini, C. Besnard, A. A. Soluyanov, and F. Baumberger, Phys. Rev. X **6**, 031021 (2016).
- [44] J. Jiang, Z. K. Liu, Y. Sun, H. F. Yang, C. R. Rajamathi, Y. P. Qi, L. X. Yang, C. Chen, H. Peng, C.-C. Hwang, S. Z. Sun, S.-K. Mo, I. Vobornik, J. Fujii, S. S. P. Parkin, C. Felser, B. H. Yan, and Y. L. Chen, Nature Communications **8**, 13973 (2017).
- [45] K. Deng, G. Wan, P. Deng, K. Zhang, S. Ding, E. Wang, M. Yan, H. Huang, H. Zhang, Z. Xu, J. Denlinger, A. Fedorov, H. Yang, W. Duan, H. Yao, Y. Wu, S. Fan, H. Zhang, X. Chen, and S. Zhou, Nature Physics **12**, 1105 (2016).
- [46] L. Huang, T. M. McCormick, M. Ochi, Z. Zhao, M.-T. Suzuki, R. Arita, Y. Wu, D. Mou, H. Cao, J. Yan, N. Trivedi, and A. Kaminski, Nature Materials **15**, 1155 (2016).
- [47] S. Zhong, A. Tiwari, G. Nichols, F. Chen, X. Luo, Y. Sun, and A. W. Tsien, Phys. Rev. B **97**, 241409(R) (2018).